Optical and structural characterization of CdS$_x$Te$_{1-x}$ thin films for solar cell applications

Optical and structural characterization of CdS_xTe_{1-x} thin films for solar cell applications

D A Wood, K D Rogers, D W Lane† and J A Coath

Cranfield University (RMCS), Shrivenham, Swindon, Wilts SN6 8LA, UK

E-mail: d.w.lane@rmcs.cranfield.ac.uk

Abstract. The optical constants have been determined for films of CdS_xTe_{1-x} over the wavelength range 250–3200 nm. The films were prepared by vacuum evaporation from solid solutions. Rutherford backscattering spectrometry has been employed to determine the thickness of the films, which is in the range 1390–2430 nm, and x-ray diffraction has been used to determine the phase and lattice parameters. The films were found to be cubic for $x < 0.65$, and hexagonal for $x > 0.65$. Reflectance and transmittance measurements have been made over the wavelength region 250–3200 nm, and a model, which includes the effects of coherent scattering, has been used to determine the complex refractive index in the transparent region. A singly subtractive Kramers–Kronig algorithm is derived for use with reflectance data of equal wavelength spacing. This novel Kramers–Kronig transform has been used to determine the optical constants in the opaque region. Polynomial functions are supplied which describe the variation of refractive index and extinction coefficient with wavelength. The photon energies required for both direct and indirect transitions have been found by least-squares fitting to the absorption spectra. The results are compared with previous work on 40 nm thick films.

1. Introduction

The almost ideal band gap and large absorption coefficient of CdTe have made this material a leading contender for use in thin-film solar cells, with commercial modules already in production. CdS is often used as a window layer, and n-CdS:p-CdTe heterojunction solar cells have reached efficiencies of 16% [1]. The next generation of cells may be designed to incorporate CdS_xTe_{1-x} layers with x between 0 and 0.5 in the absorber layer, and close to 1 in the window layer. This could reduce lattice mismatch and photocurrent loss in the window layer.

CdS–CdTe thin-film solar cells are known to possess an interfacial region of intermediate composition [2]. The overall effect of this interfacial region on cell efficiency is not yet fully understood. The region is known to accommodate the large lattice mismatch (∼10% [3]) that exists between the two materials, and may explain the absence of the band spikes predicted from the Anderson model, which would impede the flow of charge carriers. However, devices have been consistently shown [4–6] to give a reduced response at higher photon energies, and an extended response at lower energies. Interdiffusion between the layers, which results in a change in band gap, has been used to explain the resulting limited cell efficiency. Theory developed by Richardson and Hill [7] predicts a parabolic dependence of the band gap on composition. Although many workers [8–14] are in broad agreement with this, the reduction

† Author to whom any correspondence should be addressed.

in the band gap of CdTe on the introduction of sulphur into the lattice may not be significant. Hence, the extended response at lower photon energies cannot be fully explained simply in terms of the reduced band gap at low sulphur concentrations. Similarly, although the band gap of CdS reduces sharply with the introduction of tellurium into the lattice, recent work [15] has shown that the absorption coefficient of $CdS_{0.8}Te_{0.2}$ was considerably smaller than that of CdS at photon energies greater than 2.1 eV. Both of these results show that knowledge of the band gap alone is not enough for modelling the performance of CdS–CdTe solar cells—an understanding of the variation of the optical constants with wavelength is required.

Previous work [15] determined the form of the variation of the refractive index (n) and extinction coefficient (k) with wavelength for 40 nm films of CdS_xTe_{1-x}. The current work establishes the variation of n and k with wavelength for films of approximately 2 μm (the thickness of the absorber layer in typical CdS–CdTe solar cells). The spectral variation of n and k is compared with the findings of previous work, and used to ascertain the variation of band gap with composition.

2. Experimental procedure

CdS_xTe_{1-x} films were prepared by thermal evaporation from solid solutions of the required composition, the preparation of which was described in an earlier work [16]. The films were deposited at a rate of 5 nm s^{-1} onto optically flat SiO_2 held at a temperature of 200 °C. During evaporation, the substrates were held in the rotating sample holder of an Edwards Auto306 vacuum evaporator at a chamber pressure better than 1.0×10^{-5} mbar.

The film thickness was controlled approximately using a quartz thickness monitor. The thickness was later determined more precisely by observing the interference fringes on reflectance spectra.

Rutherford backscattering spectrometry (RBS) was subsequently used to confirm the thickness and composition of each sample. To achieve this, 1.6 MeV He$^+$ ions were directed at normal incidence to the samples, and the backscattered yield measured with a surface barrier detector placed at 15° to the incident beam. Spectra were collected to a total charge of 2 μC, at a beam current of 4 nA to reduce pulse pile-up. To determine the physical thickness and composition, a theoretical model was fitted to each spectrum. The film density was assumed to vary linearly across the compositional range.

The crystallographic phase and lattice parameters of each film were determined by x-ray diffraction (XRD). One-dimensional data were collected using a Siemens D500 diffractometer with a diffracted beam monochromator and Cu Kα radiation. Silicon reference material, NBS 640b, was used as an external standard. Semi-quantitative, two-dimensional intensity data were also collected using the geometry described by Wallace and Ward [17].

Measurements of the transmittance (T) and reflectance (R) were made over the wavelength range 250 nm–3200 nm with a data interval of 1 nm. This was achieved using a Perkin–Elmer Lambda-9 spectrophotometer. Reflectance was measured by diverting the beam onto the specimen at near-normal incidence and collecting the reflected component. An initial background correction was made using a standard Perkin–Elmer aluminium mirror calibrated by the National Institute of Standards, USA. Absolute values of reflectance were then obtained by correcting the measured values for the reflectance of the mirror. Transmittance measurements were also made with the beam at near-normal incidence to the sample to prevent reflected light being returned to the monochromator. Transmittance measurements were made with an uncoated substrate in the reference beam to reduce the effects of absorption bands in the silica on the measured transmittance.

3. Structural characterization

Each sample had a uniform appearance and was free from pinholes. Those with $x < 0.4$ were opaque, and thereafter the degree of optical transparency visibly increased with increasing sulphur content. A typical RBS spectrum is shown in figure 1. The low count registered beyond channel 500 confirms that the low beam current prevented pulse pile-up. The atomic density was obtained from the width of the plateau; this was converted to the physical thickness by assuming that the density of CdS_xTe_{1-x} changed linearly between CdTe and CdS. The thickness of each sample was calculated by taking an average of the values obtained by RBS and optical interference; these are provided in table 1. The two methods agreed to within 4% in all cases. RBS revealed that the composition of most samples remained unchanged between the evaporation source and the thin film. By fitting the RBS spectra, and paying close attention to the relative heights of the plateaux and the step between the Cd and Te front edges, the precision associated with the composition of each sample was estimated to be $x = \pm 0.02$. For each sample, the fit indicated that there was no change in composition with depth.
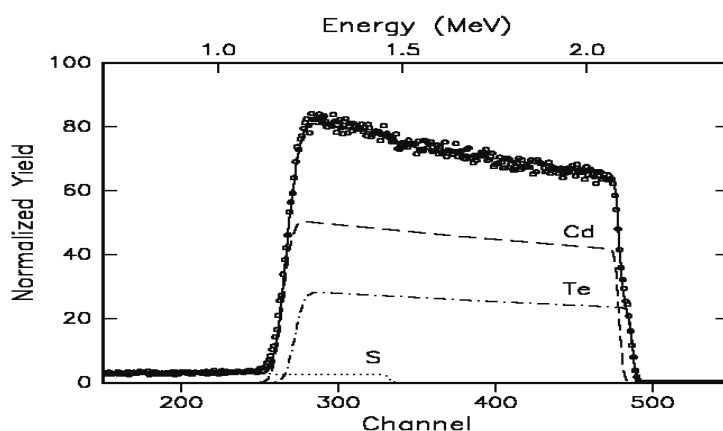

Figure 1. The RBS spectrum of $CdS_{0.5}Te_{0.5}$. Symbols represent data points and the solid line represents the simulation. Contributions from Te, Cd and S are shown.

Table 1. Composition, thickness and direct band gap for 2 μm films of evaporated CdS_xTe_{1-x}. Values in parentheses are the estimated standard deviations in the least significant figure, and are found from the fit to equation (9).

Composition (x)	Thickness (nm)	Direct band gap (eV)
0	2690	1.472(1)
0.2	2120	1.409(1)
0.3	2210	1.409(<1)
0.4	1980	1.409(<1)
0.5	1580	1.407(<1)
0.6	1450	1.390(1)
0.74	2070	1.578(<1)
0.85	1600	1.803(1)
0.93	1570	2.070(2)
1.0	1330	2.411(9)

Unambiguous crystallographic phase identification of these highly oriented films required measurements of scattering intensity out of the principal diffraction plane. Intensity data were recorded for a range of α (where α is the angle between the scattering plane and the surface normals) at a continuously increasing scattering angle, 2θ. The experimental arrangement imposed limits on α of $\sin(\phi/2)\sin\theta$, where ϕ is the angle between the incident beam and the sample surface. The data presented in figure 2 show that the $CdS_{0.5}Te_{0.5}$ sample is cubic with majority [111] orientation, and that the CdS sample is hexagonal with [001] orientation. The minor peaks close to $\alpha = 0$ in the $CdS_{0.5}Te_{0.5}$ data indicate the presence of a small number of crystallites with a different texture. In summary, the films were all polycrystalline with a cubic structure for x between 0 and 0.6, and a hexagonal structure for x between 0.74 and 1. To establish a more precise composition of the phase change, interpolation of the phase between samples was required. The method used to achieve this is described below. In contrast, the bulk equilibrium phase diagram [8, 16] shows a change in phase from cubic to hexagonal at $x = 0.2$ at 1000 °C, and a large miscibility gap at lower temperatures.
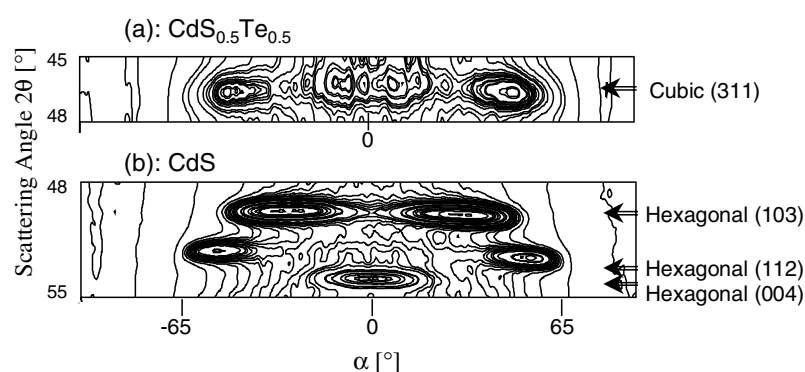

Figure 2. Intensity contours of the two-dimensional XRD data for $CdS_{0.5}Te_{0.5}$ (top) and for CdS (bottom).

Quantitative analysis of the lattice parameters and degree of preferred orientation was obtained from conventional powder diffraction data. For each sample, a set of lattice parameters describing a single crystallographic phase could be fitted to the observed Bragg maxima, in agreement with the two-dimensional data. Two typical spectra are shown in figure 3. The minor, unmarked peaks originate mostly from an x-ray tube tungsten contaminant. The cubic films were all highly [111] oriented, as illustrated in figure 3 for CdTe. The degree of preferred orientation was found to reduce with increasing sulphur content. The hexagonal films were all highly oriented in the basal plane, but with no correlation with composition. The Bragg maxima were used to determine the variation of lattice parameter with composition. These are compared to values generated from the Vegard coefficients for bulk samples, found from our previous work [16], as illustrated in figure 4 and figure 5. In the cubic case, the reduction in unit-cell volume with increasing sulphur content is less than predicted from measurements on bulk samples, while the hexagonal lattice parameters are in good agreement with the bulk case.

For the hexagonal phase, the theoretical value of c/a is 1.6331. In the current work, the value changes from 1.625 to 1.614 as the composition changes from $x = 0.74$ to $x = 1$. Figure 5 also illustrates that the values of a are slightly larger than predicted from the bulk Vegard's law, in contrast to those of c, which are in excellent agreement with Vegard's law. This indicates that the basal plane is in tension, and that the tension increases with increasing sulphur content.
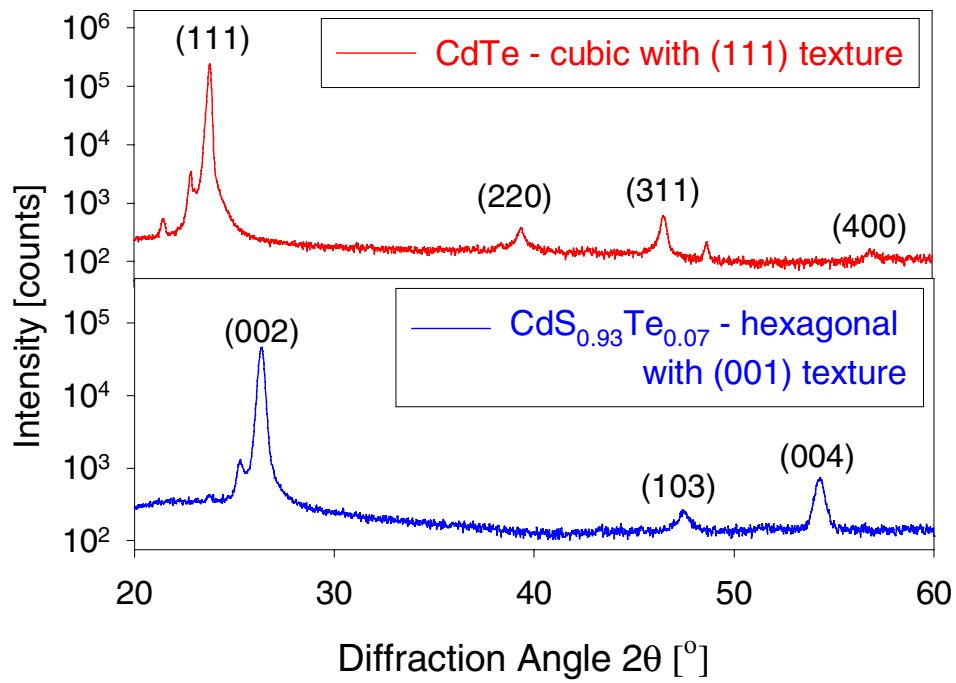
Figure 3. XRD spectra of CdTe (above) and $CdS_{0.93}Te_{0.07}$.
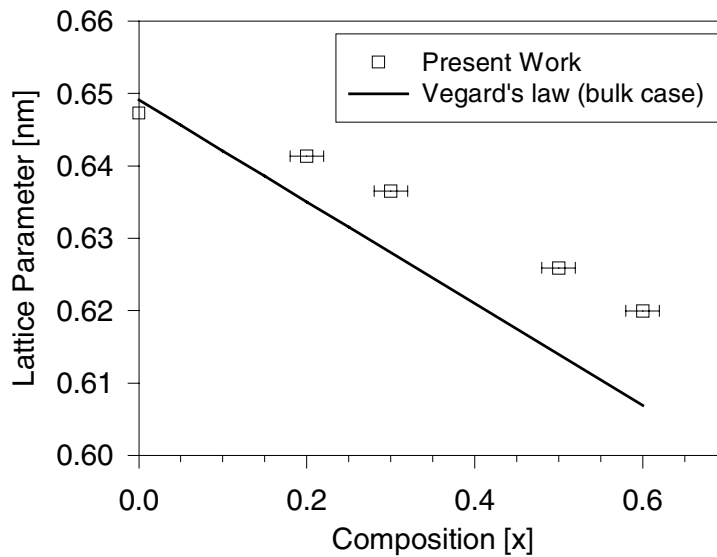

Figure 4. The variation of cubic lattice parameter with composition, compared to values from the bulk Vegard's law.

The theory developed by Hill and Richardson [18] to predict the change in band gap with composition was used successfully by Hill and Richardson [9] and by other workers [13] to predict the exact composition of any change in crystallographic phase. In this method, the
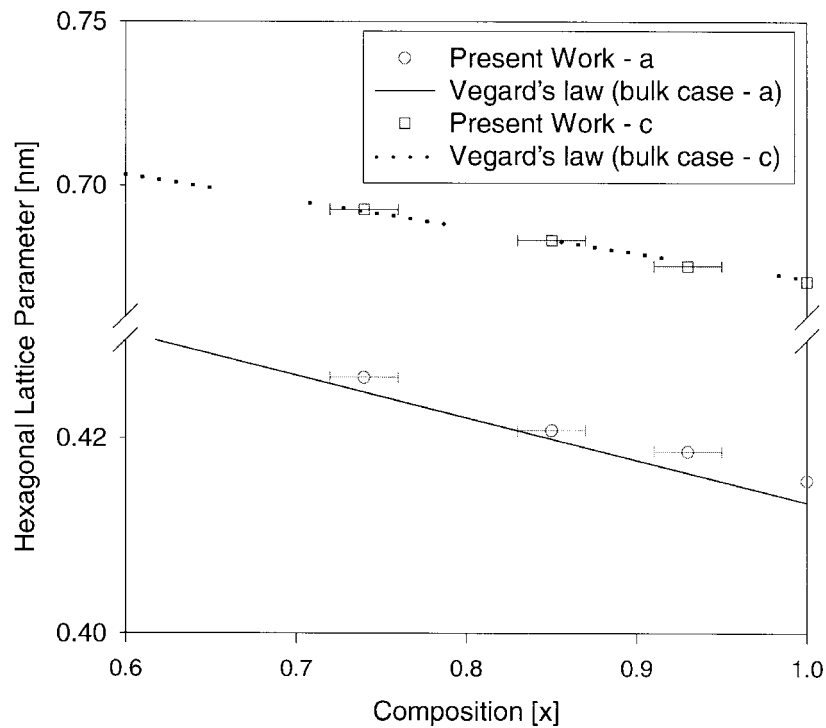
Figure 5. The variation of the hexagonal lattice parameters with composition compared to values from the bulk Vegard's law.

variation of $\Delta E(x)a^4/(1-x)$ is plotted against x for a given crystallographic phase. ΔE is the difference between the observed band gap and the band gap predicted by a linear interpolation between CdTe and CdS, and a is the lattice parameter. For any given crystallographic phase the measured values of lattice parameter are used over the compositional range where the phase is known to exist. Linearly extrapolated values of the lattice parameter are used over the remaining range. Figure 6 shows that both the hexagonal and the cubic phases show an abrupt change in gradient at $x = 0.65$, giving a more precise composition of the crystallographic phase change. The uncertainty associated with this value is estimated from the graph to be ± 0.03. This figure has only been plotted using c in the hexagonal case because changes in c/a with composition are too small to affect the graph.

4. Optical characterization

To ascertain the real and imaginary parts of the refractive index (n and k) at one discrete wavelength, a measurement is required of two optical properties. In regions where only one optical property can be measured, the spectral distribution of that property allows both parts of the complex refractive index to be calculated by the use of a Kramers–Kronig (KK) transform. In the current work, the reflectance (R) and transmittance (T) have been measured, and figure 7 shows these two quantities for the film of CdTe. It can clearly be seen that the optical properties can be split into two distinct wavelength regions. At wavelengths of greater than about 850 nm, the film is transparent, and has a number of interference fringes. At shorter
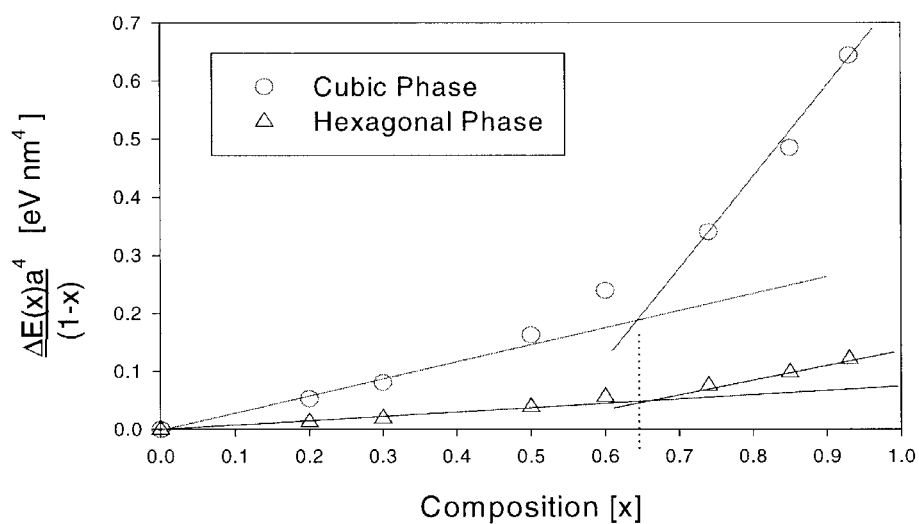
Figure 6. $\Delta E(x)a^4/(1-x)$ plotted against composition (x) for cubic and hexagonal CdS$_x$Te$_{1-x}$.
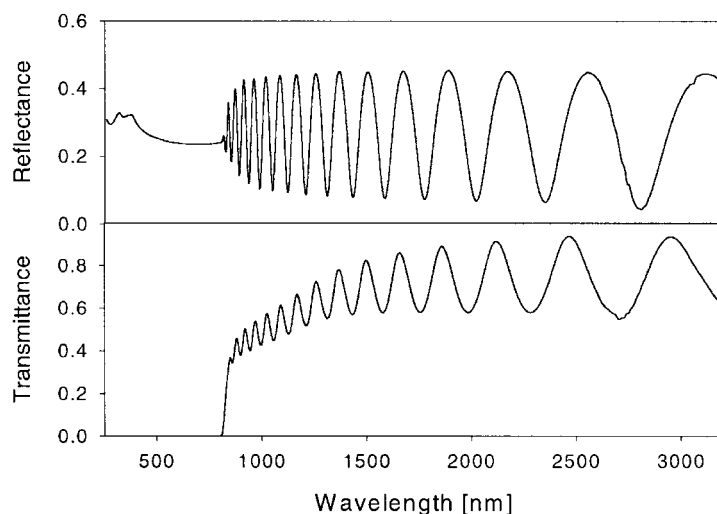
Figure 7. Reflectance and transmittance of a thin film (2690 nm) of CdTe.

wavelengths (i.e. beyond the fundamental absorption edge), the film is opaque, and only the reflectance can be measured; there is no discernible interference, although some features are present at wavelengths of less than 400 nm. Over this interval, a KK technique, described below, has been used to find the optical constants.

4.1. The transparent region: the equations of Heavens

Constructive and destructive interference within a thin film lead to a series of maxima and minima in the transmittance and reflectance. Heavens [19] has used a method of summation to derive equations describing the variation in R and T for a film on a transparent substrate as

a function of the refractive index, extinction coefficient and film thickness. These equations cannot be solved analytically, so an algorithm has been written [20] to find the refractive index (n) and extinction coefficient (k) numerically. The refractive index of the substrate was required at each wavelength, and was obtained from Palik [21].

An error analysis has been performed on the results of CdTe at a wavelength of 2260 nm, where R and T were 0.297 and 0.592 respectively. From analysis of the manufacturer's data, the measurement errors associated with these values have been estimated to be approximately 1% and 0.25% respectively. The effect of these errors on the calculated values of n and k has been found by the method of Ward [22]. The resulting maximum errors in n and k were found to be ±0.04 and ±0.009 respectively.

4.2. The opaque region: the singly subtractive Kramers–Kronig algorithm

In regions where only one parameter can be measured, measuring that parameter over an infinite wavelength range, and using a KK transform may determine the optical constants. The KK transform is used to give the phase (θ) of the complex reflectance $r = r_0 e^{i\theta}$:

$$\theta(\lambda) = \lambda \, \mathrm{P} \int_0^\infty \frac{\lambda^{*2}(\ln R(\lambda^*) - \ln R(\lambda))}{\lambda^2 - \lambda^{*2}} \, \mathrm{d}\lambda^* \tag{1}$$

where λ is the wavelength, the measured reflectance $R = |r|^2$ and P indicates the Cauchy principal value. The integrand has a singularity at $\lambda^* = \lambda$, but may be integrated numerically since it is symmetrical about this point. The value taken for the integrand at $\lambda^* = \lambda$ is simply the average of the points either side. This phase change can then be used to calculate n and k. Clearly, reflectance cannot be measured over the entire wavelength range, so an extrapolation is required for the reflectivity beyond the measured values. Results from this technique can be sensitive to the form of the extrapolation used, giving large uncertainties for the optical constants obtained. Attempts to use the ordinary KK relation for the current samples were unreliable at the low-wavelength end because the short-wavelength limit is part way through an absorption band, and the reflectance is changing rapidly. Hence it is impossible to reliably predict the form of the reflectance beyond these limits.

A modification to the KK dispersion relation, known as the singly subtractive KK relation (SSKK), was introduced by Ahrenkiel [23] in the early 1970s for use with measurements taken at equally spaced *frequency* intervals. The SSKK algorithm uses knowledge of the phase change on reflection at one wavelength—$\theta_k(\lambda_k)$—to 'anchor' the phase at this point. The ideas of Ahrenkiel have been used to derive an SSKK relation in *wavelength* space, assuming constant reflectivity beyond the measurement boundaries. On changing the variable of Ahrenkiel's formula from frequency to wavelength, we have

$$\theta(\lambda) = \frac{\lambda_k}{\lambda}\theta(\lambda_k) - \left(\frac{\lambda_k^2 - \lambda^2}{\lambda\pi}\right) \int_0^\infty \frac{\lambda^{*2} \ln R(\lambda^*)}{(\lambda^2 - \lambda^{*2})(\lambda_k^2 - \lambda^{*2})} \, \mathrm{d}\lambda^*. \tag{2}$$

If we have measurements of reflectance from λ_a to λ_b, then we may write

$$\begin{aligned}
\theta(\lambda) = {} & \frac{\lambda_k}{\lambda}\theta(\lambda_k) - \left(\frac{\lambda_k^2 - \lambda^2}{\lambda\pi}\right) \int_0^{\lambda_a} \frac{\lambda^{*2} \ln R(\lambda^*)}{(\lambda^2 - \lambda^{*2})(\lambda_k^2 - \lambda^{*2})} \, \mathrm{d}\lambda^* \\
& - \left(\frac{\lambda_k^2 - \lambda^2}{\lambda\pi}\right) \int_{\lambda_a}^{\lambda_b} \frac{\lambda^{*2} \ln R(\lambda^*)}{(\lambda^2 - \lambda^{*2})(\lambda_k^2 - \lambda^{*2})} \, \mathrm{d}\lambda^* \\
& - \left(\frac{\lambda_k^2 - \lambda^2}{\lambda\pi}\right) \int_{\lambda_b}^\infty \frac{\lambda^{*2} \ln R(\lambda^*)}{(\lambda^2 - \lambda^{*2})(\lambda_k^2 - \lambda^{*2})} \, \mathrm{d}\lambda^*.
\end{aligned} \tag{3}$$

If an assumption is made as to the form of the reflectance outside of the measurement range, then this can be substituted into the first and last integrals, which may then be solved analytically to give θ_{lo} and θ_{hi} respectively. This gives the relation

$$\theta(\lambda) = \frac{\lambda_k}{\lambda}\theta(\lambda_k) - \left(\frac{\lambda_k^2 - \lambda^2}{\lambda\pi}\right)\int_0^{\lambda_a} \frac{\lambda^{*2}\ln R(\lambda^*)}{(\lambda^2 - \lambda^{*2})(\lambda_k^2 - \lambda^{*2})}\,d\lambda^* + \theta_{lo} + \theta_{hi}. \tag{4}$$

For the assumption that the reflectance is constant outside the measurement interval:

$$\theta_{lo} = \frac{\ln R(\lambda_a)}{2\pi\lambda}\left[\lambda\ln\left(\frac{\lambda - \lambda_a}{\lambda + \lambda_a}\right) + \lambda_k\ln\left(\frac{\lambda_k + \lambda_a}{\lambda_k - \lambda_a}\right)\right]$$
$$\theta_{hi} = \frac{\ln R(\lambda_b)}{2\pi\lambda}\left[\lambda\ln\left(\frac{\lambda + \lambda_b}{\lambda_b - \lambda}\right) + \lambda_k\ln\left(\frac{\lambda_b - \lambda_k}{\lambda_b + \lambda_k}\right)\right]. \tag{5}$$

It can be seen that compared to equation (1), the SSKK integral is less dependent on the form of the extrapolation used for R. At large λ^*, the integrand varies as the inverse of λ^{*4}, compared to the inverse of λ^{*2} for the original KK relation.

In the current work $\theta(\lambda_k)$ was found by finding n and k at a wavelength, λ_k, where the material was in transition from being highly transparent to highly absorbing, and using equation (6) below:

$$\tan(\theta) = \frac{2k}{n^2 + k^2 - 1}. \tag{6}$$

In this 'transition region', transmitted radiation could still be measured, allowing the use of Heaven's equations. In this way, non-zero values of k (and hence θ) could be used. This increases the accuracy of the method by utilizing the term linear in θ in equation (4). Note that the width of this transition region reduces rapidly with increasing film thickness.

4.3. Spectral distribution of the complex refractive index

To obtain the optical constants over the entire range (250 nm–3200 nm), the results for n and k from Heaven's equations in the transparent region were used to generate the theoretical single-surface reflectance at each wavelength. These were combined with the measured values in the opaque region. The SSKK algorithm was then used to calculate n and k in the opaque region. In the transition region, where the two techniques overlapped, agreement was excellent, and well within the experimental error described in section 4.1.

The values found for n and k for three representative samples are compared to the values previously found for ultra-thin films [15] in figure 8 to figure 10. In figure 10, unlike the two preceding figures, the two films vary slightly in composition. In common with the case for the thinner films, the real part of the refractive index (n) is larger at all wavelengths for $CdS_{0.2}Te_{0.8}$ than for CdTe, but then decreases as the composition moves towards CdS. At longer wavelengths, the reduction in n as λ increases (i.e. normal dispersion) is less marked with the 2 μm films than the 40 nm films. This larger value of n at longer wavelengths leads to larger values of measured reflectance, and hence less noise associated with the measurement. The current work agrees within experimental error with Marple and Ehrenreich [24] who have measured n for CdTe using ellipsometry over the wavelength range $200 < \lambda < 700$ nm on cleaved single crystals. Myers *et al* [25] have used a similar technique to the current work to measure the optical constants for $450 < \lambda < 1900$ nm. The difference between the results of Myers *et al* and the current work is less than 3.5%, compared to around 10% for the 40 nm films.

At any given composition, the imaginary part of the refractive index (k) is lower for the 2 μm films than the 40 nm films at all wavelengths where results can be compared. The structure evident in k for CdTe is indicative of long-range order [26]. The reduction in structure
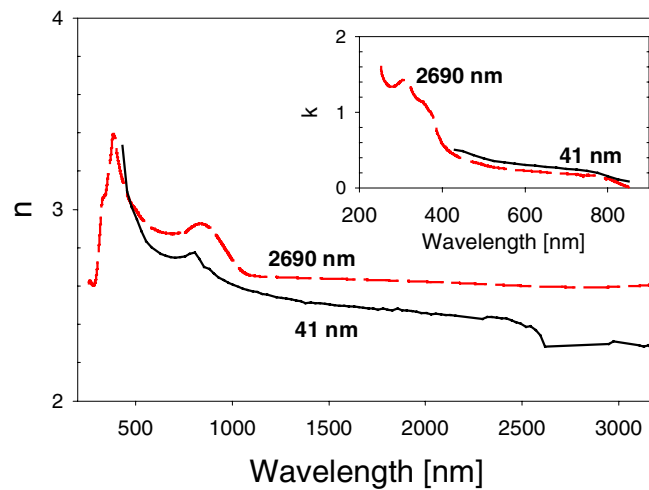
Figure 8. A comparison of the complex refractive index of a 2690 nm film of CdTe with a film of 41 nm.
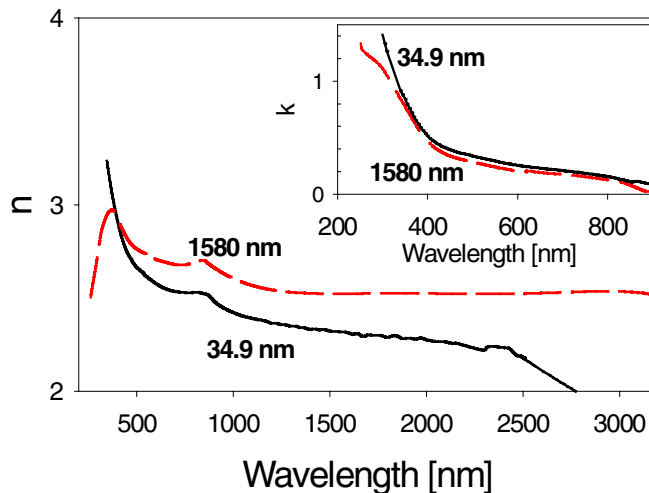
Figure 9. A comparison of the complex refractive index of a 1580 nm film of $CdS_{0.5}Te_{0.5}$ with a film of 34.9 nm.

as the series moves towards CdS could be an indication of diminishing long-range order, and may be influenced by the reducing film thickness. At the band edge, the results of Marple and Ehrenreich [24] are in agreement with the current work to within experimental error. At higher photon energies, the current work has a lower value of k, but closely follows the structure found by Myers *et al*.

Hexagonal CdS is known to be birefringent, having different optical constants according to whether the electric vector is parallel (n_e) or perpendicular (n_o) to the *c*-axis of the crystal. In the current case, with the hexagonal phase highly oriented in the [001] direction, the electric vector is perpendicular to the *c*-axis, and follows the general form of the values given for n_o and k_o by Cardona and Harbeke [27], and quoted by Palik [28], although both n and k are

Figure 10. A comparison of the complex refractive index of 1570 nm of CdS$_{0.93}$Te$_{0.07}$ with 21.4 nm of CdS$_{0.9}$Te$_{0.1}$.

about 6% lower. The values found for k decrease with wavelength for wavelengths shorter than 480 nm.

A least-squares fit for all of the data using a polynomial of order 6 has been performed, and the results can be seen in table 2 for n and table 3 for k. This allows direct comparison with the previous work [15].
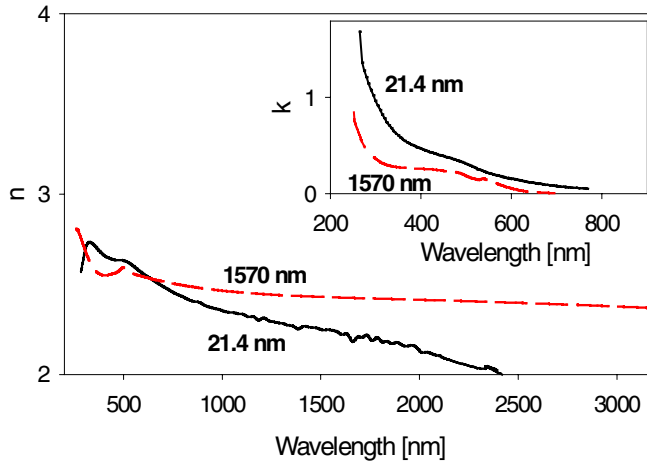
The polynomial is of the form

$$n, k = \sum_{r=0}^{6} a_r x^r. \tag{7}$$

The difference between the experimental values and the values generated by the polynomial is less than the experimental error in all cases.

4.4. Optical band gap

The method used to find the band gap has been given in detail in a previous paper [15]. The variation of absorption coefficient (α) with wavelength (λ) has been calculated using the relation

$$\alpha = \frac{4\pi k}{\lambda}. \tag{8}$$

A best fit to the function given below then yields the direct and indirect band gaps:

$$\alpha E_{pt} = k_1(E_{pt} - E_g^{\text{direct}})^{1/2} + k_2(E_{pt} - E_g^{\text{ind}})^2 \tag{9}$$

where E_{pt} is the incident photon energy, E_g^{direct} and E_g^{ind} are the direct and indirect band gaps respectively, and k_1 and k_2 are constants of proportionality related to the oscillator strength of the direct and indirect transitions. The variation of αE_{pt} has been fitted to excellent precision in all cases (see figure 11) with the coefficient of determination greater than 0.99.

Al Ani *et al* [12] found that CdS$_{0.6}$Te$_{0.4}$ had the largest absorption coefficient at an energy of 2.5 eV, while the current work found that CdS$_{0.4}$Te$_{0.6}$ was the strongest absorber at all energies studied, its absorption coefficient being slightly larger than CdTe. CdS$_{0.3}$Te$_{0.7}$ was the weakest absorber at photon energies greater than 4.5 eV. Note also that at energies greater than 2.5 eV, CdS has a considerably larger absorption coefficient than CdS$_{0.85}$Te$_{0.15}$ or CdS$_{0.93}$Te$_{0.07}$.

Table 2. Order-6 polynomial coefficients describing the variation of the refractive index (n) with wavelength for 2 μm films of $CdS_x Te_{1-x}$.

% CdS	Range (nm)	a_0	a_1	a_2	a_3
0	250–380	-1.495310×10^4	2.8343884×10^2	-2.22653500×10^0	$9.28016862 \times 10^{-3}$
	381–840	3.186990×10^1	$-2.2675234 \times 10^{-1}$	$7.33129865 \times 10^{-4}$	$-1.23483819 \times 10^{-6}$
	841–3200	1.439369×10^1	$-3.5754371 \times 10^{-2}$	$4.42047048 \times 10^{-5}$	$-2.84498102 \times 10^{-8}$
20	250–390	-5.042126×10^3	9.4667749×10^1	$-7.36557366 \times 10^{-1}$	$3.04131618 \times 10^{-3}$
	391–868	1.323223×10^2	-1.3089077×10^0	$5.52207665 \times 10^{-3}$	$-1.23764037 \times 10^{-5}$
	869–1000	6.981375×10^4	-3.6963530×10^2	$7.82559612 \times 10^{-1}$	$-8.28056051 \times 10^{-4}$
	1001–3200	-2.656367×10^{-2}	3.3046796×10^{-5}	$-2.15837496 \times 10^{-8}$	$7.77920249 \times 10^{-12}$
30	253–382	-6.034212×10^2	9.7388653×10^0	$-6.23836545 \times 10^{-2}$	$1.98716059 \times 10^{-4}$
	383–820	7.534859×10^0	$-2.3407076 \times 10^{-2}$	$4.40389976 \times 10^{-5}$	$-3.76597183 \times 10^{-8}$
	821–2850	9.684410×10^0	$-2.2103384 \times 10^{-2}$	$2.81848792 \times 10^{-5}$	$-1.88087621 \times 10^{-8}$
40	250–385	-2.155346×10^2	3.6347565×10^0	$-2.40995099 \times 10^{-2}$	$7.91231773 \times 10^{-5}$
	386–800	6.760036×10^0	$-8.6914381 \times 10^{-3}$	$-2.80712583 \times 10^{-5}$	$1.17365783 \times 10^{-7}$
	801–3200	7.947113×10^0	$-1.5637984 \times 10^{-2}$	$1.89340765 \times 10^{-5}$	$-1.20524571 \times 10^{-8}$
50	252–371	-5.850094×10^3	1.1328117×10^2	$-9.10302562 \times 10^{-1}$	$3.88679872 \times 10^{-3}$
	372–845	-2.555963×10^1	3.2866850×10^{-1}	$-1.51168392 \times 10^{-3}$	$3.58253568 \times 10^{-6}$
	846–3200	5.674763×10^0	$-7.8793190 \times 10^{-3}$	$7.73727329 \times 10^{-6}$	$-3.72654619 \times 10^{-9}$
60	253–367	-5.737537×10^2	9.4247985×10^0	$-6.16268057 \times 10^{-2}$	$2.00927018 \times 10^{-4}$
	368–830	-5.645550×10^1	6.6601339×10^{-1}	$-3.02179157 \times 10^{-3}$	$7.13136051 \times 10^{-6}$
	831–3000	5.817715×10^0	$-8.7545111 \times 10^{-3}$	$8.99141981 \times 10^{-6}$	$-4.51064939 \times 10^{-9}$
74	253–305	-9.895600×10^3	1.7610373×10^2	-1.25250608×10^0	$4.45100036 \times 10^{-3}$
	306–705	-7.144248×10^1	9.6053035×10^{-1}	$-5.02861451 \times 10^{-3}$	$1.36957047 \times 10^{-5}$
	706–3000	3.938703×10^0	$-3.6365085 \times 10^{-3}$	$3.53144237 \times 10^{-6}$	$-1.70931139 \times 10^{-9}$
85	253–470	-2.627366×10^2	4.2658408×10^0	$-2.83030953 \times 10^{-2}$	$9.95134979 \times 10^{-5}$
	471–680	1.171206×10^2	-1.1715246×10^0	$4.68764242 \times 10^{-3}$	$-9.19916300 \times 10^{-6}$
	681–3200	3.468281×10^0	$-2.0820741 \times 10^{-3}$	$1.53859486 \times 10^{-6}$	$-4.90289259 \times 10^{-10}$
93	253–268	-1.522804×10^3	1.7332850×10^1	$-6.55611798 \times 10^{-2}$	$8.22581953 \times 10^{-5}$
	269–480	-1.774680×10^1	2.9915088×10^{-1}	$-1.66561205 \times 10^{-3}$	$4.46879389 \times 10^{-6}$
	481–3200	2.981744×10^0	$-1.3298263 \times 10^{-3}$	$1.40734041 \times 10^{-6}$	$-8.25859690 \times 10^{-10}$
100	253–358	-8.260590×10^3	1.6125349×10^2	-1.30683277×10^0	$5.63089149 \times 10^{-3}$
	359–507	-4.386217×10^3	6.3421641×10^1	$-3.80849322 \times 10^{-1}$	$1.21632813 \times 10^{-3}$
	508–538	-2.957746×10^3	1.7063934×10^1	$-3.22550985 \times 10^{-2}$	$1.81567033 \times 10^{-5}$
	539–3100	2.288733×10^0	1.1704517×10^{-3}	$-2.37306406 \times 10^{-6}$	$2.16091022 \times 10^{-9}$

The energies of the indirect transitions were found to be larger than the direct ones for all of the samples, confirming that each of the samples had a direct band gap. However, the precision associated with the energy of the indirect band gap was poor compared to that of the direct band gap, and the accuracy of the fit was relatively insensitive to the value of E_g^{ind}. For this reason the values found for the indirect band gap have not been quoted. Although all of the previous workers have found that CdTe has a direct band gap, there is disagreement between workers as to the type of transitions supported by CdS.

The variation of band gap with composition is given in table 1, and is compared to the previous work on ultra-thin films [15] and to the work of Bonnet and Rabenhorst [14] in figure 12. The values for CdS and CdTe are in good agreement with those obtained by previous

Table 2. (Continued)

% CdS	Range (nm)	a_4	a_5	a_6
0	250–380	$-2.164763010 \times 10^{-5}$	$2.679985925 \times 10^{-8}$	$-1.375872809 \times 10^{-11}$
	381–840	$1.120487346 \times 10^{-9}$	$-5.042752588 \times 10^{-13}$	$8.302873057 \times 10^{-17}$
	841–3200	$1.006582844 \times 10^{-11}$	$-1.860660000 \times 10^{-15}$	$1.407040051 \times 10^{-19}$
20	250–390	$-7.029682885 \times 10^{-6}$	$8.625800164 \times 10^{-9}$	$-4.390893664 \times 10^{-12}$
	391–868	$1.549843342 \times 10^{-8}$	$-1.026764210 \times 10^{-11}$	$2.809791580 \times 10^{-15}$
	869–1000	$4.379220940 \times 10^{-7}$	$-9.260129895 \times 10^{-11}$	
	1001–3200	$-1.465656797 \times 10^{-15}$	$1.128061979 \times 10^{-19}$	
30	253–382	$-3.143722911 \times 10^{-7}$	$1.975331722 \times 10^{-10}$	
	383–820	$1.275706216 \times 10^{-11}$	$-3.949219201 \times 10^{-16}$	
	821–2850	$6.886854017 \times 10^{-12}$	$-1.307157399 \times 10^{-15}$	$1.002260891 \times 10^{-19}$
40	250–385	$-1.282788455 \times 10^{-7}$	$8.212513732 \times 10^{-11}$	
	386–800	$-1.432755699 \times 10^{-10}$	$5.992162087 \times 10^{-14}$	
	801–3200	$4.236916914 \times 10^{-12}$	$-7.785083054 \times 10^{-16}$	$5.836863637 \times 10^{-20}$
50	252–371	$-9.300094302 \times 10^{-6}$	$1.182428409 \times 10^{-8}$	$-6.241542314 \times 10^{-12}$
	372–845	$-4.652996277 \times 10^{-9}$	$3.153765072 \times 10^{-12}$	$-8.736460008 \times 10^{-16}$
	846–3200	$8.798910522 \times 10^{-13}$	$-8.144628441 \times 10^{-17}$	
60	253–367	$-3.260660557 \times 10^{-7}$	$2.105072489 \times 10^{-10}$	
	368–830	$-9.271292333 \times 10^{-9}$	$6.310971777 \times 10^{-12}$	$-1.760269015 \times 10^{-15}$
	831–3000	$1.103251259 \times 10^{-12}$	$-1.052396713 \times 10^{-16}$	
74	253–305	$-7.902377985 \times 10^{-6}$	$5.607081240 \times 10^{-9}$	
	306–705	$-2.054444799 \times 10^{-8}$	$1.613177967 \times 10^{-11}$	$-5.188879595 \times 10^{-15}$
	706–3000	$4.079265993 \times 10^{-13}$	$-3.834512278 \times 10^{-17}$	
85	253–470	$-1.959113723 \times 10^{-7}$	$2.049629388 \times 10^{-10}$	$-8.907271994 \times 10^{-14}$
	471–680	$8.872803008 \times 10^{-9}$	$-3.370519432 \times 10^{-12}$	
	681–3200	$5.615632587 \times 10^{-14}$		
93	253–268	$1.145671954 \times 10^{-9}$		
	269–480	$-5.845248860 \times 10^{-9}$	$3.004834698 \times 10^{-12}$	
	481–3200	$2.764378501 \times 10^{-13}$	$-4.978748994 \times 10^{-17}$	$3.735369747 \times 10^{-21}$
100	253–358	$-1.360745709 \times 10^{-5}$	$1.748848305 \times 10^{-8}$	$-9.339814873 \times 10^{-12}$
	359–507	$-2.178791231 \times 10^{-6}$	$2.075294019 \times 10^{-9}$	$-8.210637194 \times 10^{-13}$
	508–538	$5.110646050 \times 10^{-9}$	$-3.098069243 \times 10^{-12}$	
	539–3100	$-1.012769019 \times 10^{-12}$	$2.365951099 \times 10^{-16}$	$-2.180000884 \times 10^{-20}$

workers, as are those for solid solutions of intermediate compositions. Moving between $x = 0$ and $x = 0.6$, there is a very small reduction in band gap. Simulations [29] have shown that the associated increase in intrinsic carrier concentration has an adverse effect on the efficiency of the solar cell (assuming constant doping concentration in the absorber layer). Beyond $x = 0.6$, the band gap increases rapidly until $x = 1$. Unlike the case for ultra-thin films, the rate of increase of band gap with composition increases between $x = 0.6$ and $x = 1$. The value found for the direct band gap of CdS is slightly larger than that found by other workers. The values found for the band gap for the 2 μm films are smaller than those of the ultra-thin films apart from the case of CdS (which was the thinnest film in both cases). This may indicate the presence of stress at the interface between the film and the substrate, which dissipates as the thickness increases. The rapid increase in the band gap with increasing sulphur content after

Table 3. Order-6 polynomial coefficients describing the variation of the extinction coefficient (k) with wavelength for 2 μm films of CdS_xTe_{1-x}.

% CdS	Range (nm)	a_0	a_1	a_2	a_3
0	250–310	1.158882×10^2	-1.1783718×10^0	$4.16335814 \times 10^{-3}$	$-5.89404163 \times 10^{-6}$
	311–360	-2.996337×10^3	2.7109691×10^1	$-5.65809188 \times 10^{-2}$	$-1.43987068 \times 10^{-4}$
	361–850	1.588860×10^2	-1.5115755×10^0	$5.95814414 \times 10^{-3}$	$-1.24097984 \times 10^{-5}$
20	250–500	3.868891×10^2	-6.0639626×10^0	$3.90126935 \times 10^{-2}$	$-1.31134196 \times 10^{-4}$
	501–900	2.029439×10^2	-1.8758373×10^0	$7.21638504 \times 10^{-3}$	$-1.47395527 \times 10^{-5}$
30	250–450	3.800045×10^2	-6.2299154×10^0	$4.20388173 \times 10^{-2}$	$-1.48735408 \times 10^{-4}$
	451–800	-3.321471×10^1	3.6451859×10^{-1}	$-1.58867970 \times 10^{-3}$	$3.60935478 \times 10^{-6}$
	801–905	-4.209746×10^2	1.4554508×10^0	$-7.31277969 \times 10^{-4}$	$-3.07016839 \times 10^{-6}$
40	251–575	9.887269×10^2	-8.3896197×10^0	$2.95474310 \times 10^{-2}$	$-5.52541947 \times 10^{-5}$
	576–890	2.112251×10^2	-3.3951481×10^0	$2.24163848 \times 10^{-2}$	$-7.70098620 \times 10^{-5}$
50	253–350	5.140643×10^2	-8.2711328×10^0	$5.30803681 \times 10^{-2}$	$-1.69342265 \times 10^{-4}$
	351–700	4.654476×10^1	$-4.0267210 \times 10^{-1}$	$1.40720543 \times 10^{-3}$	$-2.45963692 \times 10^{-6}$
	701–890	1.887842×10^4	-1.4566255×10^2	$4.67644152 \times 10^{-1}$	$-7.99579190 \times 10^{-4}$
60	253–456	3.642996×10^2	-6.4431703×10^0	$4.69551059 \times 10^{-2}$	$-1.79578290 \times 10^{-4}$
	457–824	1.989748×10^1	$-1.6385062 \times 10^{-1}$	$5.56366012 \times 10^{-4}$	$-9.45602927 \times 10^{-7}$
	825–900	1.983287×10^3	-6.0678978×10^0	$1.46712166 \times 10^{-3}$	$1.29115951 \times 10^{-5}$
74	253–600	-7.531122×10^1	1.2027716×10^0	$-7.53526971 \times 10^{-3}$	$2.42082491 \times 10^{-5}$
	601–800	6.830831×10^2	-4.9994155×10^0	$1.45719690 \times 10^{-2}$	$-2.11393199 \times 10^{-5}$
85	253–550	3.194227×10^1	$-3.6012107 \times 10^{-1}$	$1.67578069 \times 10^{-3}$	$-4.11308376 \times 10^{-6}$
	551–670	-3.425208×10^2	2.4288459×10^0	$-5.15128129 \times 10^{-3}$	$-1.29905755 \times 10^{-6}$
	671–720	-1.327954×10^3	5.0078444×10^0	$-2.26082436 \times 10^{-3}$	$-1.07847735 \times 10^{-5}$
93	253–467	8.128040×10^1	-1.0302119×10^0	$5.24622749 \times 10^{-3}$	$-1.33627084 \times 10^{-5}$
	468–550	1.839333×10^4	-1.8352211×10^2	$7.31662990 \times 10^{-1}$	$-1.45687646 \times 10^{-3}$
	551–695	-9.948423×10^1	5.3524089×10^{-1}	$-4.83551658 \times 10^{-4}$	$-2.34219912 \times 10^{-6}$
100	252–349	1.370575×10^4	-2.6882504×10^2	2.19388192×10^0	$-9.53515454 \times 10^{-3}$
	350–496	-1.307697×10^3	1.9957446×10^1	$-1.26607506 \times 10^{-1}$	$4.27319042 \times 10^{-4}$
	497–526	-2.739466×10^4	1.2832293×10^2	$-5.54045636 \times 10^{-2}$	$-3.81843463 \times 10^{-4}$

$x = 0.6$ coincides approximately with the change in phase from cubic to hexagonal. In the hexagonal phase, in contrast with the cubic phase, the lattice parameters follow those predicted from the bulk Vegard's coefficients, which may indicate the absence of stress.

The thermal expansion coefficients of SiO_2 (0.5×10^{-6} K^{-1}) and of CdTe [30, 31] (4.7×10^{-6} K^{-1}), and the Young's modulus of CdTe [32] (5.12×10^{10} Pa) have been used to calculate that the thermal tensile stress of the film of CdTe is 4.8×10^7 Pa. For CdTe, the variation in band gap with pressure is known to be [30] 8×10^{-8} meV Pa^{-1}. This indicates that the band gap of CdTe should be reduced by around 4.5 meV for films prepared at 200 °C compared to those prepared at room temperature. A similar calculation for CdS, using a thermal expansion coefficient [33] of 0.5×10^{-6} and a Young's modulus [32] of 4.8×10^{10} Pa, gives a tensile stress of 2.6×10^7 Pa. The variation of band gap with pressure for CdS [34] of 4.5×10^{-8} meV Pa^{-1} gives a reduction in the band gap of 1.2 meV.

The Young's modulus of these materials is extremely anisotropic, and has been calculated from the elastic constants and the generalized Hooke's law [35] in the direction normal to the preferred orientation. This was in the basal plane in the hexagonal case, where the bond strength

Table 3. (Continued)

% CdS	Range (nm)	a_4	a_5	a_6
0	250–310	$4.27099645 \times 10^{-9}$	$-4.578806880 \times 10^{-12}$	
	311–360	$6.78040769 \times 10^{-7}$	$-6.780315976 \times 10^{-10}$	
	361–850	$1.43845442 \times 10^{-8}$	$-8.789716559 \times 10^{-12}$	$2.210233947 \times 10^{-15}$
20	250–500	$2.42707095 \times 10^{-7}$	$-2.346967558 \times 10^{-10}$	$9.274000681 \times 10^{-14}$
	501–900	$1.68257058 \times 10^{-8}$	$-1.016247830 \times 10^{-11}$	$2.533989265 \times 10^{-15}$
30	250–450	$2.91186331 \times 10^{-7}$	$-2.997207024 \times 10^{-10}$	$1.270293912 \times 10^{-13}$
	451–800	$-4.54396955 \times 10^{-9}$	$3.015420439 \times 10^{-12}$	$-8.254040864 \times 10^{-16}$
	801–905	$5.32406605 \times 10^{-9}$	$-3.260329358 \times 10^{-12}$	$7.030748822 \times 10^{-16}$
40	251–575	$5.78467085 \times 10^{-8}$	$-3.213910471 \times 10^{-11}$	$7.401414451 \times 10^{-15}$
	576–890	$1.45063995 \times 10^{-7}$	$-1.423224739 \times 10^{-10}$	$5.695475530 \times 10^{-14}$
50	253–350	$2.68518369 \times 10^{-7}$	$-1.693844708 \times 10^{-10}$	
	351–700	$2.14369018 \times 10^{-9}$	$-7.441830870 \times 10^{-13}$	
	701–890	$7.67887026 \times 10^{-7}$	$-3.927232954 \times 10^{-10}$	$8.356124388 \times 10^{-14}$
60	253–456	$3.80294098 \times 10^{-7}$	$-4.235565560 \times 10^{-10}$	$1.942012169 \times 10^{-13}$
	457–824	$7.96541008 \times 10^{-10}$	$-2.651821316 \times 10^{-13}$	
	825–900	$-1.59449166 \times 10^{-8}$	$5.653543830 \times 10^{-12}$	
74	253–600	$-4.24686097 \times 10^{-8}$	$3.879449793 \times 10^{-11}$	$-1.447286257 \times 10^{-14}$
	601–800	$1.52639121 \times 10^{-8}$	$-4.389555951 \times 10^{-12}$	
85	253–550	$5.64179402 \times 10^{-9}$	$-4.129417849 \times 10^{-12}$	$1.269939637 \times 10^{-15}$
	551–670	$1.95130358 \times 10^{-8}$	$-2.609541170 \times 10^{-11}$	$1.115952544 \times 10^{-14}$
	671–720	$1.08729898 \times 10^{-8}$	$4.451202680 \times 10^{-12}$	$-6.198501070 \times 10^{-15}$
93	253–467	$1.70146815 \times 10^{-8}$	$-8.662037922 \times 10^{-12}$	
	468–550	$1.44882383 \times 10^{-6}$	$-5.756727533 \times 10^{-10}$	
	551–695	$6.56809182 \times 10^{-9}$	$-6.380473465 \times 10^{-12}$	$2.214200294 \times 10^{-15}$
100	252–349	$2.32768786 \times 10^{-5}$	$-3.025999840 \times 10^{-8}$	$1.636593162 \times 10^{-11}$
	350–496	$-8.09173121 \times 10^{-7}$	$8.149925450 \times 10^{-10}$	$-3.410616720 \times 10^{-13}$
	497–526	$-7.34895584 \times 10^{-8}$	$1.643114737 \times 10^{-9}$	$-1.404114661 \times 10^{-12}$

is greatest, giving a large Young's modulus and a small thermal expansion coefficient. These calculations indicate that the hexagonal phase is in tension in the basal plane, in agreement with the findings of section 3.

These small changes do not explain the difference between the band gaps of the current work and either those of the ultra-thin films, or the results of Bonnet and Rabenhorst [14] (who deposited films at 180 °C). Data are not available for the variation of expansion coefficient with composition for CdS$_x$Te$_{1-x}$, which could help to explain variations in stress (and therefore band gap) with sulphur content.

5. Conclusions

Thin films ($\sim$2 μm thick) of CdS$_x$Te$_{1-x}$ prepared by thermal evaporation from solid solutions have been shown to have a direct band gap for $0 \leqslant x \leqslant 1$. The films have been shown to be cubic for $x < 0.65$, and hexagonal for $x > 0.65$. Values of n and k have been found over this compositional range for wavelengths from 250 nm to 3200 nm. In the transparent region, an
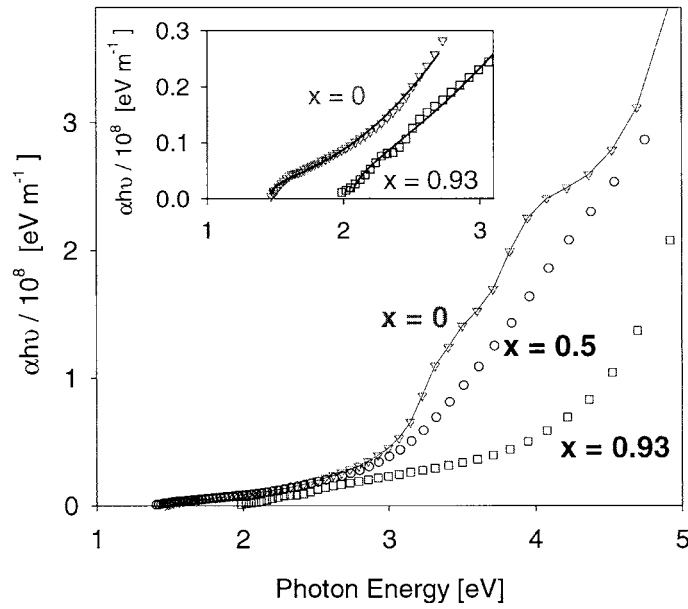
Figure 11. The variation of absorption coefficient with photon energy for 2 μm films of CdS_xTe_{1-x}. The inset shows an expanded view to illustrate the fit to equation (9), used to obtain the band gap for the samples.

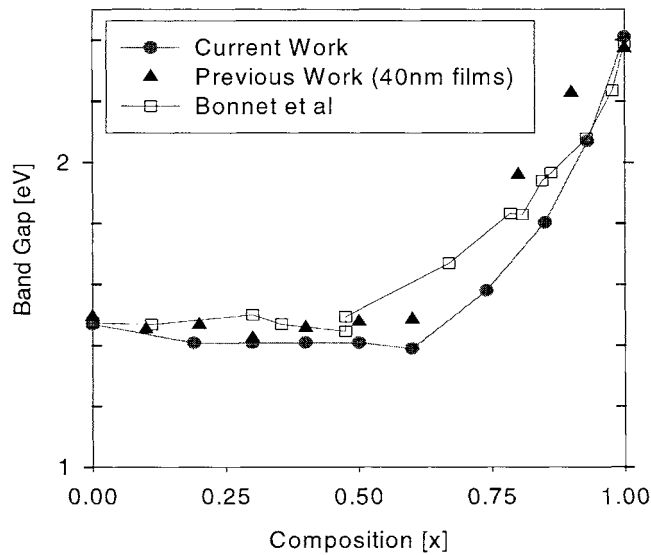**Figure 12.** The variation of the band gap of 2 μm films of CdS_xTe_{1-x} with composition.

algorithm has been used that includes the effects of coherent scatter within the films. At shorter wavelengths, where the films are opaque, a singly subtractive Kramers–Kronig technique has been employed. Equations have been presented for the SSKK algorithm in wavelength space. The variation in band gap with composition has been shown to be in agreement with those found

by previous workers and no significant change was observed between CdTe and $CdS_{0.6}Te_{0.4}$. This indicates that techniques such as photoluminescence should only be used with caution to obtain the composition in this region.

The absorption coefficient of $CdS_{0.4}Te_{0.6}$ was found to be larger than that of all other compositions at all energies studied. This result could not be predicted by considerations of the band gap alone, and indicates that this composition is suitable for use as the absorber layer in CdS–CdTe solar cells. Other compositions may also be used—$CdS_{0.5}Te_{0.5}$ has an only slightly reduced absorption coefficient compared to CdTe, and has been prepared by other workers [12] with the same crystallographic structure as CdS (i.e. wurtzite). Data presented for the variation of the optical constants with wavelength will allow the development of more precise models of the photocurrent and reflection losses for CdS–CdTe solar cells. The data will be more applicable to modelling the absorber layer in these cells, which is of a similar thickness to the samples studied, but may be combined with those from a previous study [15] of ultra-thin films more applicable to the window layer.

Acknowledgment

References

[1] Aramoto T, Kumazawa S, Higuchi H, Arita T, Shibutani S, Nishio T, Nakajima J, Tsuji M, Hanafusa A, Hibino T, Omira K, Ohyama H and Murozono M 1997 *Japan. J. Appl. Phys.* **l36** 6304

[2] Lane D W, Rogers K D, Painter J D, Wood D A and Ozsan M E 2000 *European Materials Research Symp. (Strasbourg, France, 1–4 June 1999); Thin Solid Films* at press

[3] Dhere R G, Asher S E, Jones K D, Al-Jassim M M, Moutinho H R, Rose D H, Dippo P and Sheldon P 1996 *AIP Conf. Proc.* **353** 392

[4] Birkmire R W, McCandless B E and Hegedus S S 1992 *Int. J. Solar Energy* **12** 145

[5] Clemminck I, Burgelman M, Casteleyn M and Depuydt B 1992 *Int. J. Solar Energy* **12** 67

[6] Lee J S and Im H B 1986 *J. Mater. Sci.* **21** 980

[7] Richardson D and Hill R 1972 *J. Phys. C: Solid State Phys.* **5** 821

[8] Ohata K, Saraie J and Tanaka T 1973 *Japan. J. Appl. Phys.* **12** 10

[9] Hill R and Richardson D 1973 *Thin Solid Films* **18** 25

[10] Radojcuc R, Hill A E and Hampshire M J 1981 *Solar Cells* **4** 101

[11] Moon D G and Im H B 1992 *Powder Metall.* **35** 1

[12] Al-Ani S K J, Makadsi M N, Al-Shakarchi I K and Hogarth C A 1993 *J. Mater. Sci.* **28** 251

[13] Pal R, Dutta J, Chaudhuri S and Pal A K 1993 *J. Phys. D: Appl. Phys* **26** 704

[14] Bonnet D and Rabenhorst H 1971 *Proc. Int. Conf. on the Physics and Chemistry of Semiconductor Heterojunction Layer Structures* vol 1 (Budapest: Academiai Kiado) p 119

[15] Wood D A, Lane D W, Rogers K D and Coath J A 1999 *J. Electron. Mater.* **28** 1403

[16] Wood D A, Rogers K D, Lane D W, Conibeer G J and Parton D 1998 *J. Mater. Sci. Lett.* **17** 1511

[17] Wallace C A and Ward R C 1975 *J. Appl. Crystallogr.* **8** 255

[18] Hill R and Richardson D 1973 *J. Phys. C: Solid State Phys.* **6** L115

[19] Heavens O S 1955 *Optical Properties of Thin Solid Films* (London: Butterworths) p 76

[20] Coath J A and Lovell M C 1990 *RMCS Cranfield University Report* PD/2/90

[21] Palik H R 1985 *Handbook of Optical Constants of Solids* ed E D Palik (London: Academic) p 749

[22] Ward L 1994 *The Optical Constants of Bulk Materials and Films* (Bristol: Institute of Physics Publishing) p 189

[23] Ahrenkiel R K 1971 *J. Opt. Soc. Am.* **61** 1651

[24] Marple D T F and Ehrenreich H 1962 *Phys. Rev. Lett.* **8** 87

[25] Myers T H, Edwards S W and Schetzina J F 1981 *J. Appl. Phys.* **52** 4231

[26] Jenkins T E 1995 *Semiconductor Science, Growth and Characterization Techniques* (London: Prentice-Hall) p 283

[27] Cardona M and Harbeke G 1965 *Phys. Rev.* **137** A1467

[28] Ward L 1991 *Handbook of Optical Constants of Solids II* ed E D Palik (San Diego, CA: Academic) p 579

[29] *PC1D Version 5* 1997 Photovoltaics Special Research Centre, University of New South Wales, Sydney, NSW
        2052, Australia

[30] Capper P 1994 *Properties of Narrow Gap Cadmium-Based Compounds* (London: INSPEC)

[31] Wolfe W L 1978 *Handbook of Military Infrared Technology* (Washington, DC: US Government Printing Office)

[32] Berlincourt D, Jaffe H and Shinozawa L R 1963 *Phys. Rev.* **129** 1009

[33] Cook W R Jr 1968 *J. Am. Ceram. Soc.* **51** 518

[34] Zhao X, Schroeder J, Bilodiau T G and Hwa L 1989 *Phys. Rev.* B **40** 1257

[35] Hertzberg R W 1989 *Deformation and Fracture Mechanics of Engineering Materials* (New York: Wiley) p 16